Chemical Science

ROYAL SOCIETY OF CHEMISTRY

EDGE ARTICLE

View Article Online
View Journal

Cite this: DOI: 10.1039/d5sc05778g

All publication charges for this article have been paid for by the Royal Society of Chemistry

Switchable proton conduction driven by UV/NIR-induced electron transfer in an inorganic–organic hybrid gallium phosphate–oxalate open-framework

Shuai Huang,[a] Zhihui Yi,[a] Zhuopeng Wang,[a] Tan Su,[b] Junbiao Wu,*[a] Zhiqiang Liang[b] and Jiyang Li*[b]

Conventional proton-conducting materials often fail to meet the responsiveness and flexibility required for emerging technologies such as the Internet of Things (IoT) and robotics, driving significant interest toward the development of dynamically switchable and tunable proton conductors. Herein, we present a novel UV/NIR-responsive gallium phosphate–oxalate inorganic–organic hybrid, $\{(H_3TPT)[Ga_2(H_2PO_4)_2(C_2O_4)_3]\cdot H_2PO_4\cdot H_3PO_4\}_n$ (**NEU25**, TPT = 2,4,6-tris(4-pyridyl)-1,3,5-triazine; $C_{18}N_6H_{12}$) synthesized *via* an ionothermal decomposition–reconstruction strategy within a deep eutectic solvent (DES) system. Benefiting from abundant free phosphate groups and extensive hydrogen-bonding networks, **NEU25** achieves an intrinsic proton conductivity of 6.9×10^{-4} S cm^{-1} at 20 °C and 98% relative humidity (RH). Upon UV irradiation, **NEU25** undergoes a photoinduced electron-transfer (PIET) process in which electrons are transferred from the oxalate/phosphate-based anionic framework to the protonated H_3TPT^{3+} species, producing tunable $H_3TPT^{\bullet 2+}$ π-radical aggregates that induce a distinct color change (colorless to blue) and enhance proton conductivity by nearly five-fold to 3.4×10^{-3} S cm^{-1}. These radicals also facilitate efficient photothermal conversion under low-intensity near-infrared (NIR) light (808 nm, 0.23–2.00 W cm^{-2}), elevating the temperature from room temperature to 46–99 °C. High-intensity NIR irradiation (9.75 W cm^{-2}) rapidly triggers discoloration and reverses the conductivity enhancement within 1 minute *via* photothermally induced electron retransfer. **NEU25** demonstrates good thermal and aqueous stability, rapid bidirectional photochromism, and reversible conductivity switching, offering a promising platform for remote-controlled, dynamically tunable proton conduction in next-generation smart materials and devices.

Received 31st July 2025
Accepted 5th December 2025

DOI: 10.1039/d5sc05778g

rsc.li/chemical-science

Introduction

The depletion of fossil fuels and escalating environmental concerns have intensified the need for sustainable energy solutions, positioning hydrogen fuel cells as a promising alternative.[1] Proton-conducting materials, which serve as crucial components in fuel cells, have attracted considerable interest due to their broad applications in energy conversion, chemical sensing, and bioelectronic systems.[2–4] While commercial proton exchange membranes such as Nafion[5] exhibit high conductivity (10^{-1}––10^{-2} S cm^{-1}), excellent mechanical properties, and long-term operational stability, they fall short in addressing the adaptability and responsiveness required by emerging fields such as the Internet of Things (IoT), soft electronics, and robotics. The inherent limitations of conventional materials, such as amorphous structure, high fabrication costs, poor performance under low humidity or elevated temperatures, and lack of dynamic tunability, impede both practical deployment and fundamental understanding of proton transport mechanisms. These challenges have sparked growing interest in the design of novel, dynamically switchable, and tunable proton-conducting materials that can respond to external stimuli and meet the evolving demands of next-generation technologies.

Among emerging candidates, open-framework porous materials, such as metal–organic frameworks (MOFs), covalent organic frameworks (COFs), and metalphosphate open-frameworks (MPOs), have demonstrated exceptional promise due to their structural tunability, permanent porosity, and rich functional diversity. These materials have found wide-ranging applications in catalysis,[6–8] sensing,[9,10] biomedicine,[11–13] and environmental remediation,[14] and are increasingly recognized for their potential in proton conduction.[15–17] Their crystalline

[a]Department of Chemistry, College of Sciences, Northeastern University, Shenyang, Liaoning 110819, P. R. China. E-mail: wujunbiao@mail.neu.edu.cn

[b]State Key Laboratory of Inorganic Synthesis and Preparative Chemistry, College of Chemistry, Jilin University, Changchun 130012, P. R. China. E-mail: lijiyang@jlu.edu.cn

architectures offer well-defined proton transport channels, excellent thermal and hydrolytic stability, and amenability to targeted functionalization—key attributes for next-generation solid-state proton conductors. Notably, their proton conductivities span from 10^{-2} to 10^{-8} S cm^{-1},[18] with some systems rivalling the performance of Nafion under ambient conditions. For instance, Kitagawa *et al.*[19] reported the first open-framework proton conductor, $(NH_4)_2(adp)[Zn_2(ox)_3]\cdot 3H_2O$, which exhibited a conductivity of 8×10^{-3} S cm^{-1}, establishing a foundation for this research direction. Despite these advances, the development of proton-conductive frameworks with dynamic, stimuli-responsive behavior remains in its infancy.

Stimuli-responsive open-framework porous materials have garnered increasing attention for their reversible responses to external triggers such as pH,[20] electric fields,[21] temperature,[22] solvents,[23] mechanical stress,[24] and light.[25] Among these, light-responsive systems are particularly attractive due to their non-invasive, remote-controllable nature, fast response, and high spatial resolution.[26] Notable examples include azobenzene-functionalized SURMOFs,[27] spiropyran-encapsulated ZIF-8,[28] and spiropyran-based MOF films,[29] all of which demonstrate reversible proton conductivity modulation *via* photoisomerization. While most current systems rely on such isomerization mechanisms, photoinduced electron transfer (PIET) offers an alternative strategy through the generation of tunable radicals that can enhance proton transport within hydrogen-bonded networks.[30] For instance, a 54-fold conductivity increase *via* PIET was reported by Wang *et al.*[26] MPOs have emerged as promising platforms for such applications due to their robust coordination frameworks, structural diversity, and excellent thermal stability.[31–33] Free phosphate groups and retained Brønsted acidity promote the formation of extensive hydrogen-bond networks and ensure conductivity even at elevated temperatures or low humidity.[34–36] Recent studies have demonstrated light-responsive MPOs with switchable conductivity,[30,37–39] highlighting their potential for remote-controlled proton transport. However, most systems still rely on thermal activation or irreversible structural changes, underscoring the urgent need for fast, reversible, and durable photoresponsive proton conductors for integration into next-generation smart devices.

Herein, we report the synthesis of a novel photochromic metal phosphate, $\{(H_3TPT)[Ga_2(H_2PO_4)_2(C_2O_4)_3]\cdot H_2PO_4\cdot H_3PO_4\}_n$ (**NEU25**, TPT = 2,4,6-tris(4-pyridyl)-1,3,5-triazine; $C_{18}N_6H_{12}$) *via* a decomposition–recombination strategy in a deep eutectic solvent system. The framework features abundant free phosphate groups and extensive hydrogen-bonding networks, affording high proton conductivity and excellent stability. At 20 °C and 98% RH, **NEU25** exhibits a conductivity of 6.9×10^{-4} S cm^{-1}. Upon UV irradiation, the PIET process in **NEU25** involves electron transfer from the oxalate/phosphate-based anionic framework to protonated H_3TPT^{3+}, generating tunable $H_3TPT^{\bullet 2+}$ π-radical aggregates and enhancing the conductivity by nearly five-fold to 3.4×10^{-3} S cm^{-1}, accompanied by a reversible color change from colorless to blue—outperforming many known phosphate-based proton conductors. The densely packed H_3TPT^{3+} trications in the structure promote the photogeneration of tunable $H_3TPT^{\bullet 2+}$ π-radical aggregates, which absorb strongly in the red and near-infrared (NIR) regions. Under low-intensity NIR laser irradiation (808 nm, 0.23–2.00 W cm^{-2}), the colored **NEU25** exhibits adjustable photothermal conversion, achieving surface temperatures ranging from 46 to 99 °C. High-intensity NIR exposure (9.75 W cm^{-2}, <1 min) induces rapid radical quenching and complete color fading, restoring the original low-conductivity state. This reversible dual-responsive behavior—UV-induced coloration with proton conductivity enhancement and NIR-driven fading with conductivity recovery—enables remote, contactless modulation of proton transport and offers a promising strategy for developing smart, light-regulated proton-conductive materials.

Results and discussion

Crystal structure

NEU25 was synthesized *via* an ionothermal strategy in a deep eutectic solvent (DES). The choline chloride/oxalic acid DES is indispensable for **NEU25** formation because it simultaneously dissolves and activates all precursors, provides an acidic catalytic environment, maintains a homogeneous liquid phase at 130 °C, and offers a green and efficient route unattainable with conventional solvents. Under the mildly acidic and strongly hydrogen-bonding DES environment, the neutral TPT ligand undergoes partial protonation-assisted decomposition and subsequent molecular reorganization, generating the tricationic H_3TPT^{3+} species *in situ*. This DES-mediated transformation provides a greener and more efficient alternative to using pre-synthesized *N*-alkylated TPT derivatives, while avoiding additional synthetic steps and toxic alkylation reagents (the detailed synthesis procedure and full structural and physical characterization of **NEU25** are provided in the SI).

Single-crystal X-ray diffraction analysis reveals that **NEU25** crystallizes in the monoclinic space group $P2_1/c$ (No. 14). The asymmetric unit comprises two Ga^{3+} ions, three oxalate ligands, two $H_2PO_4^-$ units, one free $H_2PO_4^-$ anion, one H_3PO_4 molecule and a fully protonated H_3TPT^{3+} trication (Fig. S1). Each Ga^{3+} ion adopts an octahedral coordination geometry, coordinated by four oxygen atoms from two oxalate ligands and two oxygen atoms from $H_2PO_4^-$ groups. Two $H_2PO_4^-$ units and two oxalate ligands bridge the Ga^{3+} centers, while the third oxalate coordinates to a single Ga^{3+} and participates in hydrogen bonding with adjacent phosphate groups and the H_3TPT^{3+} motif. The H_3TPT^{3+} cations act as charge-balancing templates and are integrated into the framework *via* hydrogen bonding and π–π interactions (Fig. 1a). Ga–O linkages and $H_2PO_4^-$ units form four-membered rings, which are further interconnected by oxalate ligands to generate infinite zigzag chains of $Ga_2(H_2PO_4)_2(C_2O_4)_3^{2-}$ (Fig. 1b). The Ga–O bond distances range from 1.869(19) Å to 2.052(19) Å, while the P–$O_{bridging}$ distances vary from 1.472(2) Å to 1.510(19) Å. The average bond lengths for the terminal groups, P=O and P–OH, are 1.492 (13) Å and 1.552(2) Å, respectively. The average C–$O_{bridging}$ and terminal C=O distances were 1.265(3) Å and 1.232(3) Å, respectively.

Hydrogen bonding plays a crucial role in assembling the three-dimensional supramolecular network. Strong N–H···O interactions between H_3TPT^{3+} and oxalate oxygen atoms exhibit donor–acceptor distances of 2.680(3)–2.886(4) Å. Likewise, O–

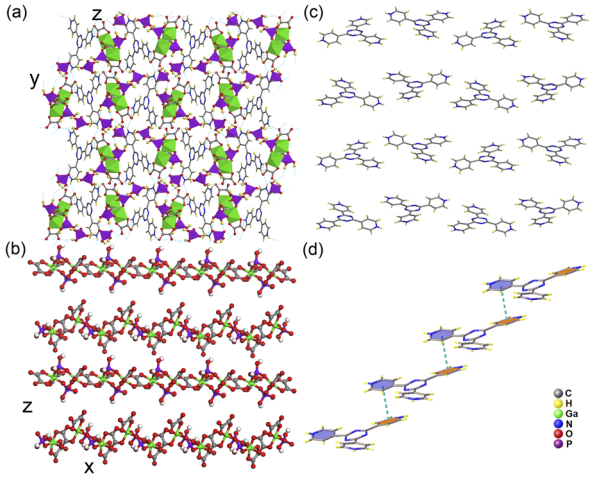

Fig. 1 (a) The infinite anionic $[Ga_2(H_2PO_4)_2(C_2O_4)_3]_n^{2n-}$ chain and the deprotonated H_3TPT^{3+} templates; (b) 1D chain structure of **NEU25**; (c) stacking pattern of TPT molecules; (d) the infinite π–π stacking interactions with face-to-face distances of 4.096 Å between adjacent H_3TPT^{3+}.

H···O interactions between phosphate and oxalate units range from 2.487(3) to 2.833(3) Å. Additional weak C–H···O interactions further reinforce the network (Table S2). The anionic $[Ga_2(H_2PO_4)_2(C_2O_4)_3]_n^{2n-}$ chains extend along the crystallographic *a*-axis. Adjacent chains are linked through extensive O–H···O hydrogen bonds involving terminal $H_2PO_4^-$ groups, forming well-defined 2D layers. These layers are further cross-linked into a 3D supramolecular architecture *via* strong hydrogen-bond interactions with both H_3PO_4 molecules and the tricationic H_3TPT^{3+} species. The pyridinium N–H groups and the P–OH groups act as complementary hydrogen-bond donors and acceptors, generating a dense and continuous hydrogen-bonded network throughout the crystal. To emphasize the density of hydrogen bonds in the **NEU25** molecule, a Hirshfeld surface analysis was conducted to elucidate intermolecular interactions, as depicted in Fig. S2a, where electron density is color-coded. The gradient from blue through white to red indicates the strength of the hydrogen bond interactions; deeper red signifies stronger interactions. This highlights the hydrogen bond donor characteristics of the system and confirms its structural stability. Furthermore, the density distributions of both N–H···O and O–H···O hydrogen bonds were calculated (Fig. S2b). The N–H···O hydrogen bond density was found to be 3.8%, while the O–H···O hydrogen bond density was found to be 45.1%, resulting in an overall hydrogen-bond contribution of 48.9%. The high density and continuity of O–H···O and N–H···O interactions form multiple, interconnected proton-hopping pathways. This dense internal hydrogen bond network renders the structure a potential proton conductor. Notably, **NEU25** exhibits a dominant face-to-face π–π stacking interaction between adjacent H_3TPT^{3+} cations, with a centroid–centroid distance of 4.096 Å (Fig. 1d and S3). These π-aggregates play a critical role in stabilizing the photo-generated $H_3TPT^{\bullet 2+}$ radicals and suppressing back-electron transfer to the anionic $[Ga_2(H_2PO_4)_2(C_2O_4)_3]_n^{2n-}$ framework.

Proton conduction and photochromism properties

The Hirshfeld surface analysis (Fig. S2) reveals that nearly half of all intermolecular contacts in **NEU25** arise from O–H···O and N–H···O hydrogen bonds (48.9% in total). This unusually high hydrogen-bond density provides continuous proton-hopping pathways along the 1D chains, across the 2D layers, and through the 3D supramolecular network. The high density of hydrogen bonds, abundant free phosphate groups, good thermal stability (>250 °C), and strong water resistance (Fig. S4 and S5) endow **NEU25** with great potential as an efficient proton conductor. To evaluate its proton conductivity, **NEU25** powders were pressed into cylindrical pellets (8 mm diameter, 6 mm thickness, 15 MPa) and tested under controlled temperature (20 °C) and humidity conditions using saturated salt solutions. AC impedance measurements were conducted, and conductivity values were extracted from Nyquist plot fitting (Schemes S1 and S2). As shown in Fig. 2a, the Nyquist plots display incomplete semicircles at high frequencies and inclined tails at low frequencies, corresponding to charge-transfer resistance and diffusion-limited processes, respectively.[40] At 35% RH, **NEU25** shows a conductivity of 7.5×10^{-7} S cm^{-1}, (Table S3) indicating intrinsic proton conduction. As humidity increases, conductivity rises significantly, reaching 6.9×10^{-4} S cm^{-1} at 98% RH—an enhancement of nearly three orders of magnitude. This performance exceeds that of most phosphonate-based proton conductors (Fig. S6a), highlighting the efficiency of its hydrogen-bonding proton transport network and the critical role of humidity in facilitating migration.

To enable external modulation, **NEU25** was irradiated with UVA light, generating the photoactivated sample **NEU25-P**. As shown in Fig. 2b and c, **NEU25-P** retains similar humidity dependence but exhibits significantly enhanced conductivity. At 98% RH, the conductivity reaches 3.4×10^{-3} S cm^{-1}—nearly five times higher than that of the pristine material—surpassing most non-switchable phosphate-based conductors. Even at 35% RH, conductivity increases modestly to 8.9×10^{-7} S cm^{-1}. The modulation range outperforms many reported light-responsive phosphate systems (Fig. S6b), suggesting a highly efficient and tunable conduction pathway. This conductivity enhancement is attributed to the formation of photogenerated π-radicals, accompanied by a distinct color change from colorless to blue (Fig. 2d and S7). *In situ* time-dependent UV-vis spectroscopy (Fig. 2e and S8) shows the gradual growth of three characteristic absorption bands at 410, 564, and 696 nm, all of which intensify and exhibit a redshift tendency with prolonged UV irradiation.[41] Kinetic analysis of the 696 nm absorption band following UVA, UVB, and UVC irradiation reveals first-order behavior, with corresponding rate constants of 0.0217, 0.0254, and 0.0239 s^{-1} (Fig. S9), confirming the rapid and efficient photoresponse of **NEU25**. Notably, **NEU25** exhibits no significant photochromism under visible light irradiation (300 W Xe lamp, $\lambda > 420$ nm). The photoinduced blue-colored **NEU25-P** reverts to its original colorless state after 24 hours at room temperature in the dark or rapidly upon heating at 80 °C for 30 minutes (Fig. 3a). Moreover, UV-vis cycling tests confirm excellent reversibility, with consistent photochromic behavior retained over at least ten UV-NIR cycles. Complementary PXRD and FT-IR

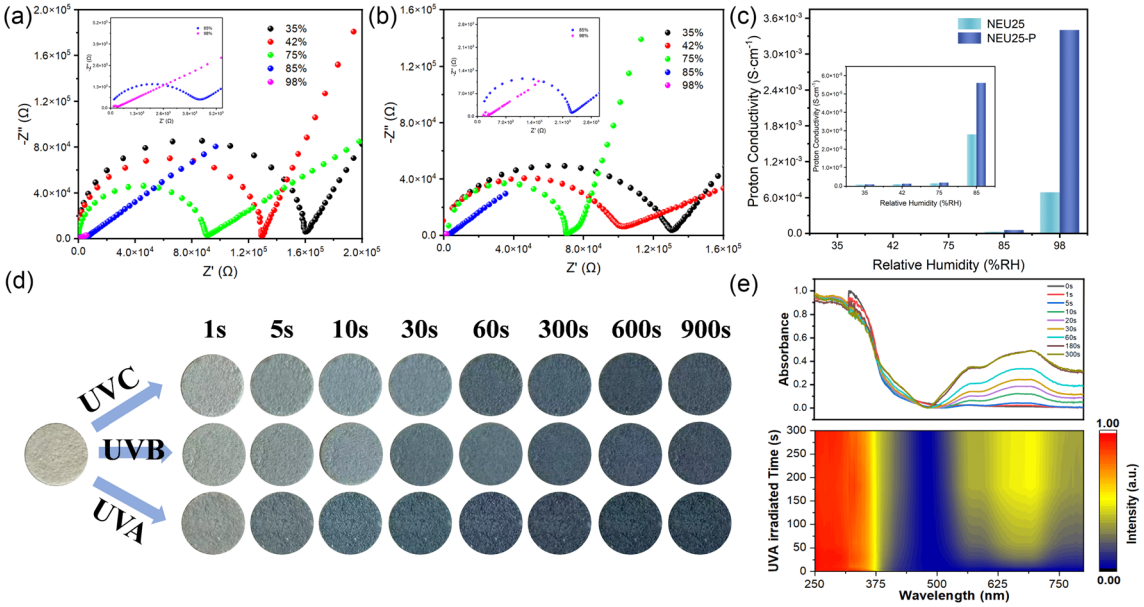

Fig. 2 (a) The Nyquist impedance plots of **NEU25** under different humidity conditions at 20 °C, with enlarged views at 85% RH and 98% RH as insets; (b) the Nyquist impedance plots of **NEU25-P** under different humidity conditions at 20 °C, with enlarged views at 85% RH and 98% RH as insets; (c) comparison of the conductivity of **NEU25** and **NEU25-P** under different humidity conditions, the inset is a magnified view of conductivity at 35–85% RH; (d) photographic images of **NEU25** exhibiting photochromic behavior under UVA, UVB, and UVC irradiation; (e) *in situ* time-resolved UV-vis spectra and contour plot of **NEU25** under UVA irradiation.

analyses further verify that the structural integrity of **NEU25** remains unaltered (Fig. S10).

Mechanistic insights

Photochromism can arise from various mechanisms, including phase transitions,[42] radical formation,[43] redox reactions,[44] isomerization,[45] and photoinduced charge transfer.[41,46–48] To elucidate the mechanism underlying the photochromic behavior of **NEU25**, PXRD and FT-IR analyses were conducted before and after UV irradiation. No observable structural or compositional changes were detected (Fig. S11 and S12), excluding the possibility of photo-induced molecular dissociation or structural rearrangement. A combination of UV-vis, ESR, and XPS measurements was performed to elucidate the photo-induced electron-transfer (PIET) process in **NEU25**. *In situ* time-dependent UV-vis spectroscopy (Fig. 2e and S8) reveals the emergence and progressive intensification of absorption bands at 410, 564, and 696 nm upon UVA irradiation. These bands display a redshift with prolonged exposure, indicating that the photogenerated species do not behave as isolated radicals but increasingly engage in intermolecular interactions. Compared with isolated $H_3TPT^{\bullet 2+}$, the redshifted profile signifies enhanced electronic coupling, consistent with π–π aggregation and hydrogen-bond-assisted stabilization of the radical cations in the crystalline environment.[41] Electron spin resonance (ESR) spectroscopy provides direct evidence of radical formation. Pristine **NEU25** shows no ESR signal, while UV-irradiated samples exhibit a single sharp isotropic peak with a *g*-value of 2.0033 (Fig. 3b and S13), characteristic of a delocalized π-type unpaired electron associated with the $H_3TPT^{\bullet 2+}$ radical species. The absence of hyperfine splitting indicates that the unpaired electron is delocalized across the conjugated TPT scaffold rather than localized on a single nitrogen atom.[49–51] The ESR signal disappears upon thermal bleaching or storage in the dark, confirming the reversible generation of $H_3TPT^{\bullet 2+}$. To further probe the electronic environment enabling PIET, X-ray photoelectron spectroscopy (XPS) was performed before and after UVA irradiation. The Ga 2p region remains unchanged (Fig. S14), confirming that the inorganic gallium phosphate–oxalate framework is not chemically perturbed during

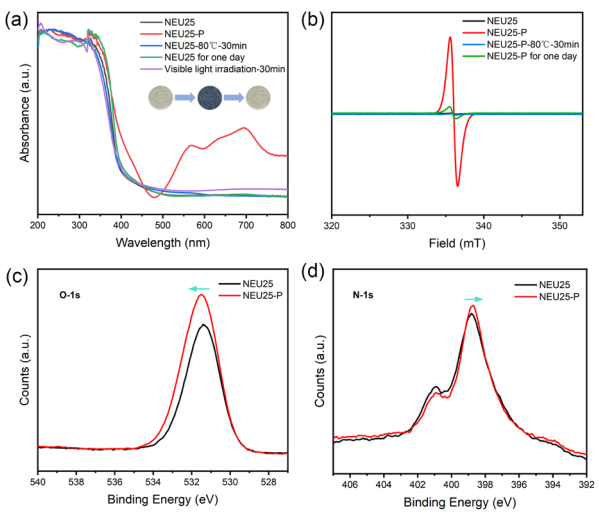

Fig. 3 (a) UV-vis spectra of **NEU25** after UV irradiation, thermal treatment at 80 °C for 30 minutes, storage in the dark for one day and visible light irradiation for 30 min. (b) ESR spectra of compound **NEU25** under various light/thermal stimuli; XPS core-level spectra of **NEU25** before and after UV irradiation: (c) O 1s; (d) N 1s.

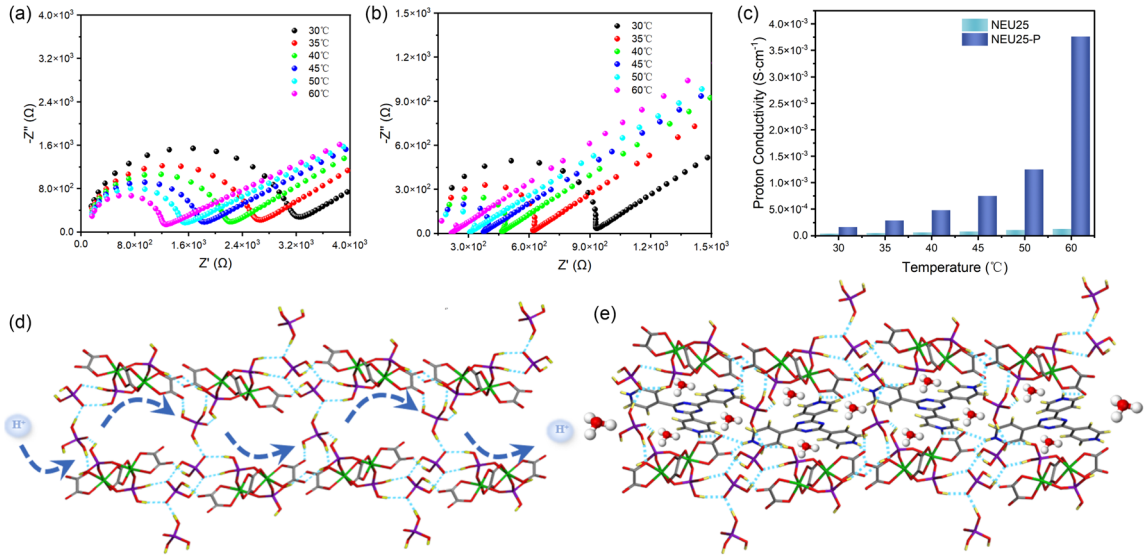

Fig. 4 (a) Nyquist impedance plots of **NEU25** under different temperature conditions at 85% RH; (b) Nyquist impedance plots of **NEU25-P** under different temperature conditions at 85% RH; (c) comparison of the conductivity of **NEU25** and **NEU25-P** at different temperatures; (d) proton transport pathway of **NEU25** (the TPT molecule has been eliminated); (e) proton transport pathway of **NEU25-P**.

photoexcitation. Minor shifts (<0.2 eV) in the O 1s and N 1s regions (Fig. 3c and d) reflect subtle electronic rearrangements within the protonated H_3TPT^{3+} ligand but do not directly detect the radical, which is unstable under X-ray irradiation. Instead, the XPS results support the presence of an electron-deficient, protonated ligand that readily accepts an electron upon UV excitation, serving as the electronically activated precursor for PIET. The photogenerated radical is further stabilized by structural features intrinsic to **NEU25**. Face-to-face π–π stacking between adjacent H_3TPT^{3+} units (centroid–centroid distance = 4.096 Å) and the dense network of O–H···O and N–H···O hydrogen bonds enhance electronic coupling and suppress rapid back-electron transfer. This structural arrangement rationalizes both the redshifted radical absorption and the reversible photochromism. Together, these results establish a coherent PIET mechanism involving protonation-enabled electronic activation, UV-driven electron transfer from the inorganic framework, formation of the $H_3TPT^{\bullet 2+}$ radical cation, and intermolecular stabilization *via* π–π stacking and hydrogen bonding. This mechanism fully accounts for the reversible photochromism and the light-modulated proton-conductivity enhancement observed in **NEU25**.

To elucidate the proton conduction mechanism of **NEU25**, temperature-dependent conductivity measurements were conducted at 85% RH in the range of 30–60 °C (Fig. 4a). The conductivity increased from 4.1×10^{-5} S cm^{-1} to 1.3×10^{-4} S cm^{-1} (Table S4), indicating a 3.2-fold enhancement. This temperature dependence suggests a thermally activated transport process. Arrhenius fitting yielded an activation energy (E_a) of 0.36 eV (Fig. S15a), consistent with a Grotthuss mechanism, where protons migrate *via* hydrogen-bond networks through successive hopping.[52–54] The dense hydrogen-bonding network formed by free phosphate groups (Fig. 4d) facilitates such proton transport. To evaluate the effect of UV irradiation, the same measurements were performed on UV-treated **NEU25-P**. As shown in Fig. 4b, **NEU25-P** displayed significantly higher conductivity across the temperature range, with a notably larger enhancement factor compared to the pristine material (Fig. 4c). The corresponding E_a increased to 0.85 eV (Fig. S15b), suggesting a transition to a Vehicle mechanism,[55–57] in which protons migrate as hydronium ions (H_3O^+) *via* water-assisted pathways. This shift is attributed to UV-induced electron depletion on the nitrogen atoms of TPT, which reduces proton affinity and facilitates proton release. Under humid conditions, the liberated protons form H_3O^+ and diffuse through the hydrogen-bond network (Fig. 4e), further enhancing conductivity. Although the static crystal structure of **NEU25** lacks large pores, TGA measurements (Fig. S16) on samples equilibrated at 98% RH reveal a water uptake of ∼8.75%, confirming the presence of sufficient interstitial or surface-adsorbed water to generate H_3O^+ in localized domains. The considerably higher E_a observed for **NEU25-P** therefore reflects a highly confined vehicle-type process, where hydronium migration is restricted within narrow hydrogen-bonded regions, rather than long-range diffusion through open channels. This confined transport model reconciles the structural compactness of **NEU25** with the observed photo-enhanced proton conductivity.

Photothermal response and NIR-triggered switching

Structural analyses of **NEU25** reveal the presence of infinite π-aggregates, which facilitates the generation of photoinduced π-aggregate radicals ($H_3TPT^{\bullet 2+}$) and exhibit distinct absorption bands in the red and near-infrared regions.[58–62] UV-vis-NIR spectroscopy (200–2000 nm) confirmed this behavior, with new absorption bands appearing after UV irradiation (Fig. 5a), consistent with the formation of densely packed $H_3TPT^{\bullet 2+}$ radicals *via* a PIET. Leveraging this tunable NIR absorption, the photothermal response of UV-activated **NEU25-P** was

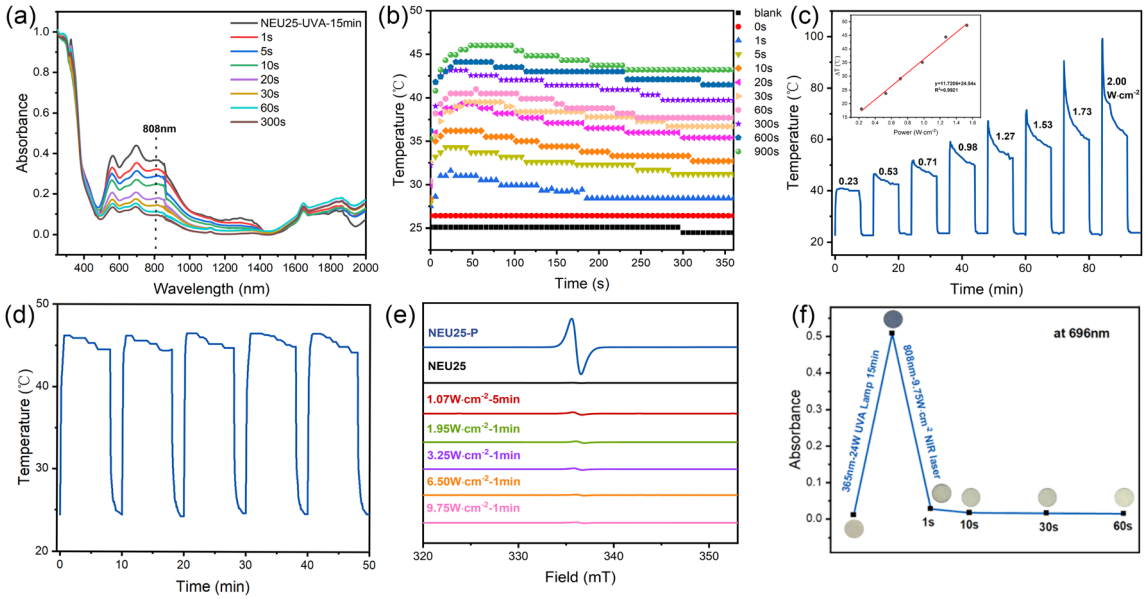

Fig. 5 (a) Time-dependent UV-vis-NIR spectra of **NEU25-UVA-15min** under 808 nm NIR irradiation at a power density of 1.07 W cm^{-2}; (b) photothermal conversion curves of **NEU25-UVA** films with different UV response times under NIR laser irradiation (808 nm, 0.23 W cm^{-2}); (c) temperature rise of the **NEU25-UVA-1min** film under different NIR laser intensities. The inset illustrates the relationship between the average temperature rise (ΔT) and the NIR laser power; (d) ESR spectra of **NEU25** under irradiation with different 808 nm laser power densities; (e) absorbance changes of **NEU25** at 696 nm in the UV-vis spectrum under 808 nm laser irradiation (inset shows the color changes of **NEU25** before and after bleaching induced by UVA irradiation and NIR exposure); (f) Nyquist plots for **NEU25**, **NEU25-P**, and **NEU25-NIR-1min** (20 °C and 85% RH).

investigated. **NEU25** powders were deposited as thin films (1 cm × 1 cm) on quartz substrates, pre-irradiated with UVA light for various durations, and then exposed to an 808 nm NIR laser (0.23 W cm^{-2}, approximating 1.6–2.0 × sunlight intensity). As the UVA exposure increased from 1 s to 15 min, the surface temperature rose from 31 °C to 46 °C (Fig. 5b), consistent with the progressive formation of $H_3TPT^{\bullet 2+}$ radicals. Reflecting this pronounced photothermal response, **NEU25** displays a solar-to-thermal conversion efficiency of 59.7%, highlighting the strong heat-generation capability of the stabilized radical aggregates. In contrast, unirradiated **NEU25** and bare quartz showed negligible temperature increases (2.4 °C and 1.7 °C, respectively). Notably, **NEU25-UVA-15min** reached 46 °C within 30 s under constant NIR irradiation, indicating efficient photothermal conversion. A linear relationship was observed between the final temperature and UVA exposure time (Fig. S17), enabling precise thermal control. Photothermal behavior was further evaluated under varying NIR laser powers. As shown in Fig. 5c, the conversion temperature could be modulated bidirectionally by adjusting both the UVA duration and laser intensity. At powers above 0.53 W cm^{-2}, rapid thermal fading occurred, likely due to partial quenching of $H_3TPT^{\bullet 2+}$ radicals back to H_3TPT^{3+}, reducing absorption and photothermal efficiency. Cycling tests confirmed that **NEU25-UVA-15min** maintained stable performance over five irradiation cycles (Fig. S18), and extended exposure revealed only a slight decline in maximum temperature from 46.5 °C to 43.3 °C (Fig. S19), indicating a dynamic equilibrium after partial fading.

Given **NEU25**'s responsiveness to low-power NIR laser irradiation, its fading behavior was systematically examined. Upon exposure to an 808 nm laser at 1.07 W cm^{-2} (7–10 × sunlight intensity), the **NEU25-UVA-15min** sample underwent a visible blue-to-colorless transition within seconds (Fig. S20). UV-vis spectra showed 63.3% and 67.0% decreases in absorbance at 564 and 696 nm, respectively, while ESR signals declined in parallel (Fig. 5d). At 1.95 W cm^{-2}, the 696 nm absorbance dropped by 82.8% in just 10 s, accompanied by a pronounced reduction in ESR intensity (Fig. S21), indicating accelerated fading. Higher power irradiation (3.25, 6.50, and 9.75 W cm^{-2}) was further explored. At 9.75 W cm^{-2}, complete fading occurred within 1 s (Fig. S22 and Movie S1), with a 94.6% drop at 696 nm and near-complete ESR quenching (Fig. S23 and Fig. 5d), confirming ultrafast radical deactivation. PXRD and IR analyses verified that the **NEU25** structure remained intact after 1 min of laser exposure across all power levels (Fig. S24), indicating that the fading process is dominated by photothermal radical quenching rather than photodamage. Given this reversible optical behavior, the impact on proton conductivity was investigated. Conductivity measurements at 20 °C and 85% RH showed that the UV-activated **NEU25-P** sample exhibited enhanced conductivity, which dropped from 5.6 × 10^{-5} S cm^{-1} to 2.4 × 10^{-5} S cm^{-1} following 1 min of 9.75 W cm^{-2} laser irradiation (Fig. 5f), nearly reverting to the original value observed for pristine **NEU25**. PXRD analysis of post-conduction samples confirmed structural stability and phase purity under humid conditions (Fig. S25). These findings highlight **NEU25**'s capability for reversible, non-contact optical modulation of proton conductivity, positioning it as a promising candidate for chemical sensing and other applications requiring tunable ionic transport.

Conclusions

In summary, a novel inorganic–organic hybrid MPO was synthesized in a cost-effective deep eutectic solvent (DES) system. The framework incorporates abundant free phosphate groups and an extensive hydrogen-bonding network, enabling efficient proton transport with a conductivity of 6.9×10^{-4} S cm^{-1} at 20 °C and 98% relative humidity. Upon UV irradiation, a photoinduced electron transfer (PIET) process generates π-radicals, leading to a five-fold conductivity enhancement (up to 3.4×10^{-3} S cm^{-1}) and a reversible color change from colorless to blue—surpassing the performance of most phosphate-framework proton conductors. The photogenerated radicals also impart strong absorption in the NIR region, enabling efficient photothermal conversion under low-power 808 nm laser irradiation (0.23–2.00 W cm^{-2}), with surface temperatures tunable from room temperature to 99 °C. Notably, high-power NIR exposure (9.75 W cm^{-2}, <1 min) induces rapid radical quenching and decolorization and restores the original low-conductivity state, completing a reversible UV-enhanced/NIR-recovered optical switching cycle. Collectively, this study establishes an effective approach for achieving non-contact, bidirectional optical regulation of ion transport in solid-state proton conductors. The synergistic combination of intrinsic proton conductivity, UV/NIR responsiveness, and structural robustness makes **NEU25** a promising candidate for light-gated protonic circuitry, remotely controlled fuel-cell components, smart ion-transport membranes, and adaptive photothermal or chemical sensing systems.

Author contributions

Shuai Huang: investigation, methodology, data curation, formal analysis, validation, and writing – original draft. Zhihui Yi: investigation, methodology. Zhuopeng Wang: formal analysis, validation, and writing – review & editing. Tan Su: formal analysis, validation, and writing – review & editing. Junbiao Wu: investigation, conceptualization, supervision, validation, funding acquisition, writing – original draft, and writing – review & editing. Zhiqiang Liang: investigation and writing – review & editing. Jiyang Li: investigation, funding acquisition, and writing – review & editing. All authors have given approval to the final version of the manuscript.

Conflicts of interest

There are no conflicts to declare.

Data availability

CCDC 2442358 contains the supplementary crystallographic data for this paper.[63]

The data supporting this article have been included as part of the supplementary information (SI). Supplementary information: SI section, tables, figures, and movies. See DOI: https://doi.org/10.1039/d5sc05778g.

Acknowledgements

This work was financially supported by the Fundamental Research Funds for the Central Universities of China (N25LPY026) and the Basic Scientific Research Program of the Education Department of Liaoning Province (JYTMS20230624). Special thanks are due to the Analytical and Testing Center, Northeastern University for instrumental analysis.

References

1 S. J. Hamrock and M. A. Yandrasits, *J. Macromol. Sci. Polym. Rev.*, 2006, **46**, 219–244.
2 K.-D. Kreuer, S. J. Paddison, E. Spohr and M. Schuster, *Chem. Rev.*, 2004, **104**, 4637–4678.
3 M. R. Karim, K. Hatakeyama, T. Matsui, H. Takehira, T. Taniguchi, M. Koinuma, Y. Matsumoto, T. Akutagawa, T. Nakamura, S. Noro, T. Yamada, H. Kitagawa and S. Hayami, *J. Am. Chem. Soc.*, 2013, **135**, 8097–8100.
4 Y. Deng, E. Josberger, J. Jin, A. F. Roudsari, B. A. Helms, C. Zhong, M. P. Anantram and M. Rolandi, *Sci. Rep.*, 2013, **3**, 2481.
5 K. A. Mauritz and R. B. Moore, *Chem. Rev.*, 2004, **104**, 4535–4585.
6 K.-G. Liu, Z. Sharifzadeh, F. Rouhani, M. Ghorbanloo and A. Morsali, *Coord. Chem. Rev.*, 2021, **436**, 213827.
7 Y.-S. Wei, M. Zhang, R. Zou and Q. Xu, *Chem. Rev.*, 2020, **120**, 12089–12174.
8 A. Bavykina, N. Kolobov, I. S. Khan, J. A. Bau, A. Ramirez and J. Gascon, *Chem. Rev.*, 2020, **120**, 8468–8535.
9 H.-Y. Li, S.-N. Zhao, S.-Q. Zang and J. Li, *Chem. Soc. Rev.*, 2020, **49**, 6364–6401.
10 W. Chen, J. Wang, L. Zhao, W. Dai, Z. Li and G. Li, *J. Alloys Compd.*, 2018, **750**, 895–901.
11 Z. Wang, Q. Sun, B. Liu, Y. Kuang, A. Gulzar, F. He, S. Gai, P. Yang and J. Lin, *Coord. Chem. Rev.*, 2021, **439**, 213945.
12 S. A. A. Razavi and A. Morsali, *Coord. Chem. Rev.*, 2020, **415**, 213299.
13 R. Fang, A. Dhakshinamoorthy, Y. Li and H. Garcia, *Chem. Soc. Rev.*, 2020, **49**, 3638–3687.
14 S. Rojas and P. Horcajada, *Chem. Rev.*, 2020, **120**, 8378–8415.
15 S.-S. Bao, K. Otsubo, J. M. Taylor, Z. Jiang, L.-M. Zheng and H. Kitagawa, *J. Am. Chem. Soc.*, 2014, **136**, 9292–9295.
16 X.-S. Xing, Z.-H. Fu, N.-N. Zhang, X.-Q. Yu, M.-S. Wang and G.-C. Guo, *Chem. Commun.*, 2019, **55**, 1241–1244.
17 X. Chen and G. Li, *Inorg. Chem. Front.*, 2020, **7**, 3765–3784.
18 X. Meng, H.-N. Wang, S.-Y. Song and H.-J. Zhang, *Chem. Soc. Rev.*, 2017, **46**, 464–480.
19 M. Sadakiyo, T. Yamada and H. Kitagawa, *J. Am. Chem. Soc.*, 2009, **131**, 9906–9907.
20 K. Zhou, H. Liu, S. Zhang, X. Huang, Y. Wang, G. Huang, B. D. Sumer and J. Gao, *J. Am. Chem. Soc.*, 2012, **134**, 7803–7811.
21 G. Wang, X. Chen, S. Liu, C. Wong and S. Chu, *ACS Nano*, 2016, **10**, 1788–1794.
22 S. Chae, J. P. Lee and J. Kim, *Adv. Funct. Mater.*, 2016, **26**, 1769–1776.

23 G. Xi, L. Sheng, J. Du, J. Zhang, M. Li, H. Wang, Y. Ma and S. X.-A. Zhang, *Nat. Commun.*, 2018, **9**, 4819.
24 X. Sun, J. Zhang, X. Lu, X. Fang and H. Peng, *Angew. Chem., Int. Ed.*, 2015, **54**, 3630–3634.
25 J. Park, D. Feng, S. Yuan and H. Zhou, *Angew. Chem., Int. Ed.*, 2015, **54**, 430–435.
26 X.-S. Xing, C. Sun, L. Liu, M.-S. Wang and G.-C. Guo, *CCS Chem.*, 2021, **3**, 50–57.
27 K. Müller, J. Helfferich, F. Zhao, R. Verma, A. B. Kanj, V. Meded, D. Bléger, W. Wenzel and L. Heinke, *Adv. Mater.*, 2018, **30**, 1706551.
28 H. Liang, Y. Guo, Y. Shi, X. Peng, B. Liang and B. Chen, *Angew. Chem., Int. Ed.*, 2020, **59**, 7732–7737.
29 A. B. Kanj, A. Chandresh, A. Gerwien, S. Grosjean, S. Bräse, Y. Wang, H. Dube and L. Heinke, *Chem. Sci.*, 2020, **11**, 1404–1410.
30 Q. Zhang, W.-J. Wei, Q. Li, J. Pan, S.-D. Han, J.-X. Hu and G.-M. Wang, *Sci. China:Chem.*, 2021, **64**, 1170–1176.
31 M. Inukai, Y. Nishiyama, K. Honjo, C. Das, S. Kitagawa and S. Horike, *Chem. Commun.*, 2019, **55**, 8528–8531.
32 A.-J. Liu, Y. Han, F. Xu, S.-D. Han, J. Pan and G.-M. Wang, *Dalton Trans.*, 2020, **49**, 14598–14604.
33 S. M. Haile, *Acta Mater.*, 2003, **51**, 5981–6000.
34 L. Vilčiauskas, M. E. Tuckerman, G. Bester, S. J. Paddison and K.-D. Kreuer, *Nat. Chem.*, 2012, **4**, 461–466.
35 S. Zhang, Y. Lu, X.-W. Sun, Z. Li, T.-Y. Dang, Z. Zhang, H.-R. Tian and S.-X. Liu, *Chem. Commun.*, 2020, **56**, 391–394.
36 D. Umeyama, S. Horike, M. Inukai, T. Itakura and S. Kitagawa, *J. Am. Chem. Soc.*, 2012, **134**, 12780–12785.
37 C. Jia, S. Liang, Y.-X. Wen, Z.-Z. Xue, J. Pan, J.-X. Hu and G.-M. Wang, *Cryst. Growth Des.*, 2024, **24**, 2202–2209.
38 G.-M. Li, F. Xu, S.-D. Han, J. Pan and G.-M. Wang, *Inorg. Chem.*, 2022, **61**, 8379–8385.
39 X. Ren, F. Chen, C. Zhang, Z. Liang, X. Yu, S. Han and G. Wang, *Chem.–Eur. J.*, 2024, **30**, e202402581.
40 H. Farahani, R. Wagiran and G. A. Urban, *IEEE Sens. J.*, 2021, **21**, 9657–9666.
41 N. Zhang, Y. Han, M. Du, R. Sa, M. Wang and G. Guo, *Chem.–Eur. J.*, 2019, **25**, 13972–13976.
42 N. Kida, M. Hikita, I. Kashima, M. Okubo, M. Itoi, M. Enomoto, K. Kato, M. Takata and N. Kojima, *J. Am. Chem. Soc.*, 2009, **131**, 212–220.
43 S. Roy, S. P. Mondal, S. K. Ray and K. Biradha, *Angew. Chem., Int. Ed.*, 2012, **51**, 12012–12015.
44 M. Wang, G. Guo, W. Zou, W. Zhou, Z. Zhang, G. Xu and J. Huang, *Angew. Chem., Int. Ed.*, 2008, **47**, 3565–3567.
45 J. Harada, T. Fujiwara and K. Ogawa, *J. Am. Chem. Soc.*, 2007, **129**, 16216–16221.
46 L.-Z. Cai, Q.-S. Chen, C.-J. Zhang, P.-X. Li, M.-S. Wang and G.-C. Guo, *J. Am. Chem. Soc.*, 2015, **137**, 10882–10885.
47 X. Li, J. Yang and Y. Yang, *Mater. Chem. Front.*, 2023, **7**, 1463–1481.
48 S. Han, J. Hu and G. Wang, *Coord. Chem. Rev.*, 2022, **452**, 214304.
49 T. Yamase and E. Ishikawa, *Inorg. Chem.*, 2022, **61**, 13743–13755.
50 A. Chemseddine, C. Sanchez, J. Livage, J. P. Launay and M. Fournier, *Inorg. Chem.*, 1984, **23**, 2609–2613.
51 T. Yamase, *J. Chem. Soc., Dalton Trans.*, 1987, 1597.
52 D.-W. Lim and H. Kitagawa, *Chem. Rev.*, 2020, **120**, 8416–8467.
53 K.-D. Kreuer, *Chem. Mater.*, 1996, **8**, 610–641.
54 N. Agmon, *Chem. Phys. Lett.*, 1995, **244**, 456–462.
55 K. Kreuer, A. Rabenau and W. Weppner, *Angew Chem. Int. Ed. Engl.*, 1982, **21**, 208–209.
56 P. Ramaswamy, N. E. Wong and G. K. H. Shimizu, *Chem. Soc. Rev.*, 2014, **43**, 5913–5932.
57 X. Meng, H.-N. Wang, S.-Y. Song and H.-J. Zhang, *Chem. Soc. Rev.*, 2017, **46**, 464–480.
58 Y. Wang, M. Frasconi, W.-G. Liu, Z. Liu, A. A. Sarjeant, M. S. Nassar, Y. Y. Botros, W. A. Goddard and J. F. Stoddart, *J. Am. Chem. Soc.*, 2015, **137**, 876–885.
59 Y. Wang, M. Frasconi and J. F. Stoddart, *ACS Cent. Sci.*, 2017, **3**, 927–935.
60 T. Chen, H.-B. Jiang, K.-B. Jiang, D.-L. Hu, L.-Z. Cai, M.-S. Wang and G.-C. Guo, *ACS Appl. Mater. Interfaces*, 2022, **14**, 11619–11625.
61 J. Jung, W. Liu, S. Kim and D. Lee, *J. Org. Chem.*, 2019, **84**, 6258–6269.
62 P. Liao, J. Li, J. Liu, Q. Xiong, Z. Ruan, T. Li, W. Deng, S. Jiang, J. Jia and M. Tong, *Angew. Chem., Int. Ed.*, 2024, **63**, e202401448.
63 CCDC 2442358: Experimental Crystal Structure Determination, 2025, DOI: 10.5517/ccdc.csd.cc2mzgrv.